Computer Simulations of Stellar-Coronagraph Observations

Itoh, Yoichi
Takato, Naruhisa
Takami, Hideki
Tamura, Motohide

(Citation)
Publications of the Astronomical Society of Japan,50(1):55-65

(Issue Date)
1998-02

(Resource Type)
journal article

(Version)
Version of Record

(URL)
https://hdl.handle.net/20.500.14094/90001440

PASJ: Publ. Astron. Soc. Japan **50**, 55–65 and Plate 2 (1998)

Computer Simulations of Stellar-Coronagraph Observations

Yoichi ITOH
Department of Astronomy, School of Science, The University of Tokyo, 7-3-1 Hongo, Bunkyo-ku, Tokyo 113-0033
E-mail(YI): yitoh@pavane.mtk.nao.ac.jp

Naruhisa TAKATO, Hideki TAKAMI, and Motohide TAMURA
National Astronomical Observatory, 2-21-1 Osawa, Mitaka, Tokyo 181-8588

(Received 1997 September 3; accepted 1997 November 12)

Abstract

An infrared camera optimized for stellar coronagraphic observations is now under construction for use on the Subaru 8 m telescope. This instrument, called CIAO (Coronagraphic Imager with Adaptive Optics), aims to observe faint infrared objects in the very close vicinity of a bright source, such as brown dwarfs in binary systems and protoplanetary disks. We have conducted extensive computer simulations in order to optimize the transmittance patterns of the stellar coronagraph components and to evaluate the performance of the camera for various astronomical objects. The simulations took into account atmospheric turbulence and telescope aberration, where the wavefront is expanded in terms of Zernike polynomials. We examined the effect of the truncation of the Zernike expansion to the properties of the resultant PSFs, and found that the higher terms of the Zernike expansion omitted by former studies should be included rather in the simulation for coronagraphic observations than in the simulation for direct imaging observations. The results of the simulations show that a few minute integrations will be required for the detection of a young brown dwarf in a binary system in the Pleiades, while it will take a few nights for a protoplanetary disk in the Taurus molecular cloud.

Key words: Infrared: general — Instruments — Stars: binaries — Stars: pre–main-sequence

1. Introduction

It is well known that a coronagraph is a powerful instrument for investigating very faint objects in the close vicinity of bright objects. Originally, Lyot (1939) developed a coronagraph to observe solar corona and prominences without solar eclipses. The key components of the coronagraph are an occulting mask and a Lyot stop (cf. figure 1). The occulting mask is located at the first focal plane, and obscures the light from a central bright source. Subsequently blocked is the diffracted light from the pupil of the telescope and the occulting mask by the Lyot stop, which is centered on the optical axis in the pupil plane. Finally, we detect the image at the second focal plane, where the light from the central source is almost suppressed. Therefore, a faint object in a very close vicinity of the bright source can be detected.

Such traditional coronagraphs have provided fruitful results not only in solar science, but also in stellar astronomy. The most striking result was obtained by Smith and Terrile (1984), who discovered a circumstellar dust disk around the main-sequence star β Pic using an optical stellar coronagraph with a $7''$ diameter mask. However, the conventional-type coronagraph has been limited in spatial resolution by seeing, as well as telescope tracking error and aberration. These problems make it difficult to employ the small occulting masks needed to study the very close vicinity of a central bright object.

Recent progress concerning the adaptive optics technique enable us to use smaller occulting masks. Nakajima et al.(1995) discovered the cool brown dwarf Gl 229B using the Johns Hopkins University Adaptive Optics Coronagraph (Golimowski et al. 1992) mounted on the Palomar 60 inch telescope. The system consists of an image stabilizer and an optical stellar coronagraphic camera employing a $4''$ diameter mask. However, the wavefront compensation by an adaptive optics system is currently not sufficient at optical wavelengths. Infrared observations with a large-diameter telescope and an adaptive optics system make it possible to observe faint infrared objects in the very close vicinity of the central source by employing masks smaller than the seeing limit. Under the average seeing conditions at Mauna Kea, an 8 m telescope with adaptive optics systems will provide images with $0\farcs07$ resolution at the K band (2.2 μm), allowing us to use an occulting mask as small as a few tenths of an arcsecond in diameter.

In order to detect such faint objects near to bright

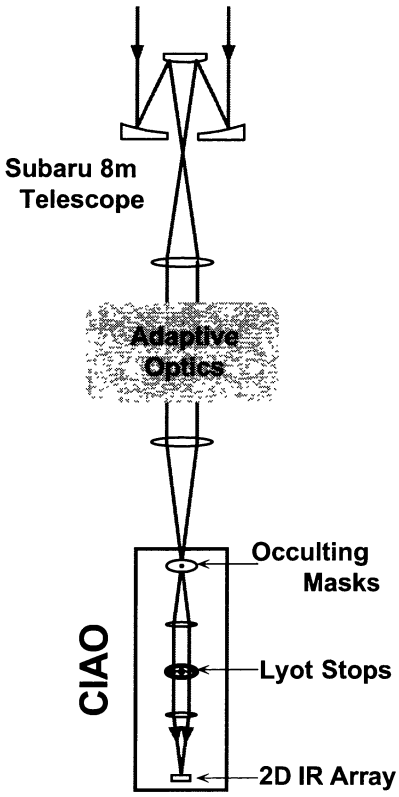

Fig. 1. Schematic optical layout for the stellar coronagraphic observations. The observational system consists of three parts: the Subaru 8.2 m telescope, the adaptive optics system, and the infrared stellar coronagraph camera (CIAO). The details of CIAO are described in Tamura et al.(1995).

sources, an infrared camera optimized for stellar coronagraphic observations, called CIAO (Coronagraphic Imager with Adaptive Optics), is proposed for the use on the Japanese Subaru 8.2 m telescope now under construction atop of Mauna Kea, Hawaii (Tamura et al. 1995). CIAO is to be used at near-infrared (1–5 μm) wavelengths, because (1) an adaptive optics system compensates any wavefront distortion effectively at near-infrared wavelengths, and (2) the optical aberration, including scattered light is smaller at near-infrared wavelengths than that in the visible region. Also, great care should be taken to determine the transmittance pattern of the occulting masks and the Lyot stops in order to increase the performance of halo suppression, as well as using a simple optics design for minimizing any scattered light and ghost images, dust cleaning of the optical surfaces, and the mechanical structure. CIAO is now under construction, and the first observation will be conducted in 1998. To find the optimum sizes and transmittance patterns of the occulting masks and the Lyot stops, as well as to evaluate the performance of this instrument, we have carried out extensive computer simulations and laboratory experiments. Here, we present the results of computer simulations for stellar coronagraphic observations.

Although many studies for stellar coronagraphic observations by computer simulations have been conducted so far, most of them were proposed for a space telescope (e.g., Breckinridge et al. 1982; Malbet et al. 1995). Because no considerations are necessary for atmospheric aberration, the results of these studies cannot be directly applied to ground-based observations. Only a few calculations have been made for ground-based stellar coronagraphic observations (Ftaclas et al. 1994; Nakajima 1994; Malbet 1996). However, as we show later in section 2, the number of terms of the Zernike expansion used in the previous simulations was not sufficient to simulate the intensities of the halo of the coronagraphic PSF. We have included a sufficient number of terms to produce a realistic halo, which is essential for evaluating the performance of the coronagraph in detecting, for instance, a faint protoplanetary disk.

We carried out a computer simulation of a stellar coronagraphic observation including a sufficient number of terms of a Zernike expansion to evaluate the halo component, and then calculated PSFs for ground-based stellar coronagraphic observations. In section 2, we describe our simulation method. The effect of truncation of the Zernike expansion is carefully discussed. The transmittance patterns of the occulting mask and the Lyot stop are discussed in section 3. In section 4, we discuss the possibilities of detecting young brown dwarfs in binary systems and protoplanetary disks. Our results are summarized in section 5.

2. Simulation Method

Figure 1 shows schematics of optical layout of CIAO. The assumptions and simulation method used in our calculation were as follows. The light from an object is monochromatic and incoherent. The atmospheric structure is a single layer represented by the Kolmogorov phase structure function. The distortion of the primary mirror of the telescope is considered in terms of the structure function. The adaptive optics system has a 36-element deformable mirror and compensates any wavefront distortion (Takami et al. 1997). The circular pupil is obscured by the secondary mirror and the secondary mirror support of the Subaru telescope. The simulated field of view corresponds to $2\farcs2 \times 2\farcs2$ for K-band observations on a 512×512 grid ($0\farcs0043$/pix). The diameter of the pupil is divided into 40 pixels. Lightwave propagation between the pupil and the focal plane by a mirror or a lens is represented by a fast Fourier transformation. We used a two-dimensional fast Fourier transformation (FFT) in the calculations. The error due to FFT on the finite square grid was not significant in this simulation.

A workstation, HP 735 with a 128 MB memory was used for the calculations.

Turbulence due to the atmosphere and the aberration of the primary mirror are considered for the wavefront distortion at the pupil plane. We assume the Kolmogorov structure function as atmospheric turbulence, where the phase structure function $D_\Phi(\rho)$ is represented as

$$D_\Phi(\rho) = 6.88\left(\frac{\rho}{r_0}\right)^{5/3}, \tag{1}$$

where r_0 is the Fried parameter (Fried 1965). For most cases, we assume $D/r_0 = 5.0$, where D is the diameter of the telescope (8.2 m for the Subaru telescope). This value corresponds to the expected median seeing of 0.″45 at Mauna Kea. The covariance of the Kolmogorov turbulence has been described by Noll (1976) and the implementation for simulations was made by Roddier (1990), where the wavefront is expanded in terms of Zernike polynomials with normalized random coefficients. The notation for the Zernike polynomial index j is as follows:

$$\begin{aligned} Z_{\mathrm{even}j} &= \sqrt{n+1}\,R_n^m(r)\sqrt{2}\cos(m\theta), && m \neq 0, \\ Z_{\mathrm{odd}j} &= \sqrt{n+1}\,R_n^m(r)\sqrt{2}\sin(m\theta), && m \neq 0, \\ Z_j &= \sqrt{n+1}\,R_n^0(r), && m = 0, \end{aligned} \tag{2}$$

where

$$R_n^m(r) = \sum_{s=0}^{(n-m)/2} \frac{(-1)^s(n-s)!}{s!\,[(n+m)/2-s]!\,[(n-m)/2-s]!}\,r^{n-2s} \tag{3}$$

and n and m denote the radial and angular indices, respectively. The Wiener power spectrum of the phase fluctuations in the Kolmogorov atmosphere is described as equation (21) in Noll (1976). The coefficients of the Zernike expansion (a_{atm}) is also given as equation (25) in Noll, assuming a Gaussian random variation with zero mean. Following Roddier, we generate independent random coefficients for the Karhunen-Loève expansion.

The distortion of the primary mirror under the operation of the active supports of the Subaru telescope is also considered. The structure function of the primary mirror with the active support derived from the polish specification $D_{\mathrm{s}}(r)$ is represented as

$$D_{\mathrm{s}}(r) = a_1(1 - e^{-b_1^2x^2}) + a_2(1 - e^{-b_2^2x^2}), \tag{4}$$

where $x = r/D$, $D = 820$ cm, $a_1 = 0.0001714$, $b_1^2 = 390.87$, $a_2 = 0.00005360$, $b_2^2 = 237593.8$. The Wiener spectrum of the primary mirror $\Phi_{\mathrm{s}}(k)$ is represented as

$$\Phi_{\mathrm{s}}(k) = \sum_{i=1}^{2} \frac{4\sqrt{\pi}Ra_i}{b_i} e^{-(\frac{2\pi R}{b_i})^2k^2}. \tag{5}$$

The covariance of the coefficients of the Zernike expansion (a_{tcl}) is described using a hypergeometric function,

$$\begin{aligned} &\langle (a_{\mathrm{tcl}})_j (a_{\mathrm{tcl}})_{j'} \rangle \\ &= \int \tilde{Z}_j^*(k)\frac{1}{R^2}\,\Phi_{\mathrm{s}}\left(\frac{k}{R}\right)\tilde{Z}_{j'}(k)\,dk \\ &= (-1)^{\frac{n+n'-2m}{2}} 2\sqrt{(n+1)(n'+1)} \sum_{i=1}^{2} \frac{a_i}{b_i} \\ &\quad \times \int_0^\infty \frac{J_{n+1}(x)J_{n'+1}(x)}{x} e^{-x^2/b_i^2}\,dx \\ &= (-1)^{\frac{n+n'-2m}{2}} 2^{-(n+n'+1)} \sqrt{(n+1)(n'+1)} \\ &\quad \times \frac{\Gamma\left(\frac{n+n'+3}{2}\right)}{\Gamma(n+2)\Gamma(n'+2)} \sum_{i=1}^{2} a_i b_i^{n+n'+1} \\ &\quad \times {}_3F_3\left(\frac{n+n'+3}{2}, \frac{n+n'+4}{2}, \frac{n+n'+3}{2}; \right. \\ &\qquad\qquad \left. n+2, n'+2, n+n'+3; b_i^2\right) \\ &\quad \times \delta_{mm'}, \end{aligned} \tag{6}$$

where $\tilde{Z}$ is the Fourier transformation of the Zernike polynomial, J_n is the nth order Bessel function of the first kind and ${}_3F_3$ is a hyper geometric function.

We derive the coefficients of Zernike polynomial a_j as follows:

$$a_j = (a_{\mathrm{atm}})_j + (a_{\mathrm{tcl}})_j. \tag{7}$$

Iterations 1000 times were carried out in our simulations. The operation of the adaptive optics system is modeled by eliminating the first 20th terms in the Zernike expansion, though, in practice, residual errors still remain within the first 20th terms and the wavefront is corrected to some degree, even beyond the 20th term. Although the Zernike expansion has an infinite number of terms, the maximum term of the Zernike expansion ($j_{\max}$) is fixed to be 1200, due to the computational limitation.

It is therefore necessary to examine how much this truncation affects the properties of the resultant PSFs. Roddier has discussed this in terms of the structure function of the wavefront, and concluded that the truncation after 496 Zernike terms produces only a negligible error. Nakajima and Haniff (1993) also argued for truncating of the Zernike expansion after a finite number of terms. They concluded that the Zernike expansion truncated at the 300th term is sufficient in the calculation, and that the results are good to 5% in the focal plane PSF. We have re-examined the truncation effect. Figure 2 shows the PSFs for the cases of truncating the Zernike expansion at $j = 100$, $j = 500$, and $j = 1200$. For the PSF without a coronagraph, as mentioned by

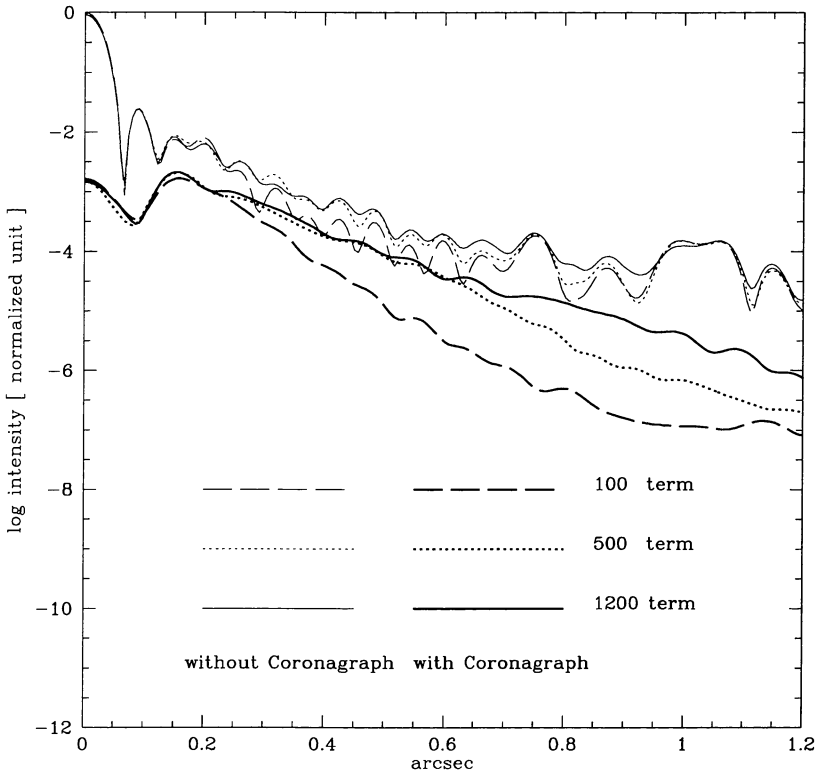

Fig. 2. PSFs of a single point source for the various truncations of the Zernike expansions. $D/r_0 = 5.0$ is assumed. The adaptive optics system is assumed to compensate for any wavefront distortion up to the 20th term of the Zernike expansion. The thin lines represent the observations without a stellar coronagraph, and the thick lines represent observations with a stellar coronagraph. For both cases, the dashed lines, the dots, and the solid lines represent the calculations where of the Zernike expansion are truncated at the 100th, 500th, and 1200th terms, respectively. The bumps of the PSFs are mainly caused by diffraction light of the telescope pupil pattern.

Roddier and by Nakajima and Haniff, a calculation truncated at the 500th term of the Zernike expansion is sufficient, while a calculation truncated at the 100th term can not produce an accurate PSF. However, this is not the case for calculating stellar coronagraphic observations. Because the lower frequency components of the wavefront are suppressed by the occulting mask at the first focal plane, at the second focal plane the higher frequency components significantly contribute to the halo compared with a direct imaging observation. Even for a calculation with $j_{\max} = 500$, the radius of the area calculated correctly seems to be about 0.″6. Because the number of the radial node in the wavefront represented by the Zernike expansion is roughly proportional to the square root of the index of the Zernike expansion (j), the radius of the area where the PSF is calculated correctly grows almost proportional to $\sqrt{j_{\max}}$. Even for $j_{\max} = 1200$, as in the case simulated below, the area should be restricted to the region of 0.″9 radius from the center. We therefore limit ourselves to the area $r < 0.''9$ for the discussions below.

In our computer simulations for astronomical observations, we generate the wavefront from the objects as follows. For a system consisting of two point sources (such as the brown-dwarf companion discussed below), the intensity of the companion object is generated by multiplying that of the primary object, while the phase of the companion is shifted at random in the focal plane. For a diffuse object around a central point source (such as in the case of the protoplanetary disk observation discussed in subsection 4.2), we execute the same procedure as for the case of two-point systems, but for each pixel.

3. Optimizing Stellar-Coronagraph Components

Several combinations of sizes and transmittance patterns have been proposed for occulting masks and Lyot stops. We derive the optimal shape of these stellar coronagraph components by computer simulations, which take into account the atmospheric turbulence and telescope distortion.

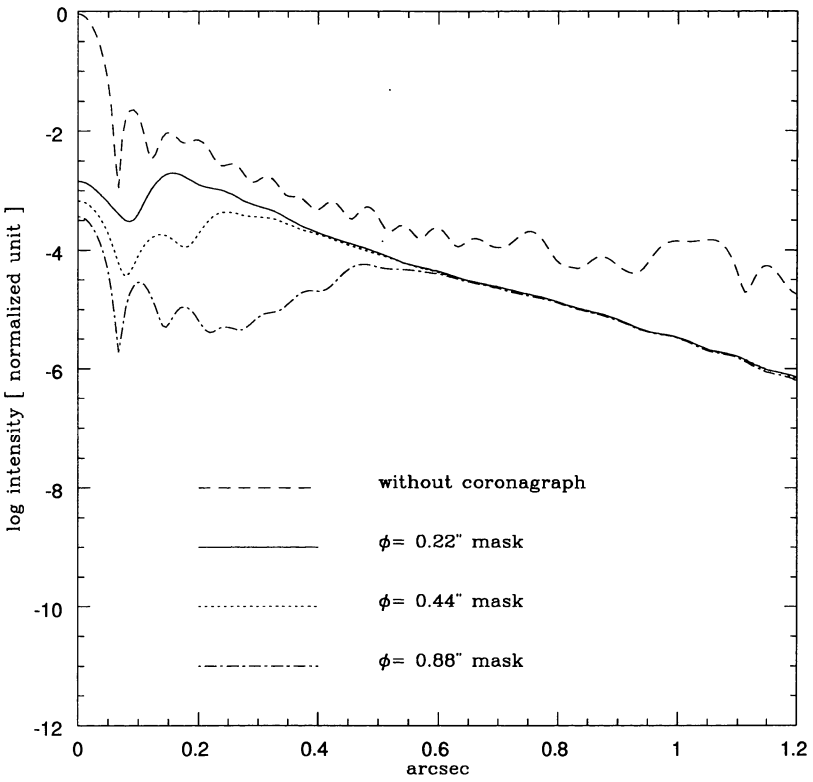

Fig. 3. Effect of the diameter of the occulting mask simulated for a single point source. The dashed line represents the PSF without stellar coronagraph. The PSF using stellar coronagraph with 0.″22 diameter mask, 0.″44 diameter mask, and 0.″88 diameter mask are shown by the solid, the dot lines, and the dot-dashed line, respectively. No significant differences are seen in the resultant PSFs, especially at the halo.

3.1. Occulting Mask

We carried out simulations to evaluate the effect of an occulting mask to the PSF of the final image. The most effective Lyot stop (see subsection 3.2) is used.

First, the diameter of the occulting mask alone does not affect the halo. We consider a 0.″22 diameter mask, a 0.″44 diameter mask, and a 0.″88 diameter mask. The transmittance patterns are binary pattern. The resultant PSFs are shown in figure 3, where no significant difference in halo is seen in any of the masks.

The transmittance pattern of the mask also does not affect the halo. We consider three transmittance patterns of occulting masks. The transmittance patterns are the binary pattern, Gaussian pattern, and apodized pattern (Gaussian smoothed binary pattern) with a diameter of 0.″22 ($4\lambda/D$) for all cases:

$$\left.\begin{aligned} T_{\mathrm{m1}}(r) &= 0 \quad \left(r \le \frac{a}{2}\frac{\lambda f}{D}\right) \\ T_{\mathrm{m1}}(r) &= 0.955 \quad \left(r > \frac{a}{2}\frac{\lambda f}{D}\right) \end{aligned}\right\} \text{for binary pattern,} \quad (8)$$

$$T_{\mathrm{m2}}(r) = 1 - 0.955 \exp\left[-\frac{r^2}{\left(\frac{a}{2}\frac{\lambda f}{d}\right)^2}\right] \quad \text{for Gaussian pattern, and} \quad (9)$$

$$T_{\mathrm{m3}}(r) = T_{\mathrm{m1}}(r) * \exp\left[-\frac{r^2}{\left(b\frac{\lambda f}{D}\right)^2}\right] \quad \text{for apodized pattern,} \quad (10)$$

where $T_{\mathrm{m}}(r)$ is the amplitude transmittance at radius r, λ is the observed wavelength, f is the focal length, D is the diameter of the telescope, a is an effective diameter of the mask fixed to $a\frac{\lambda}{D} = 0.''22$, and b is a constant. Assumed is a mask whose transmittance is not zero, even at the center of the mask. Such a mask enables us to measure the centroid of the central object. The results are shown in figure 4. A binary mask and an apodized mask permit one to use the central source as a flux calibrator.

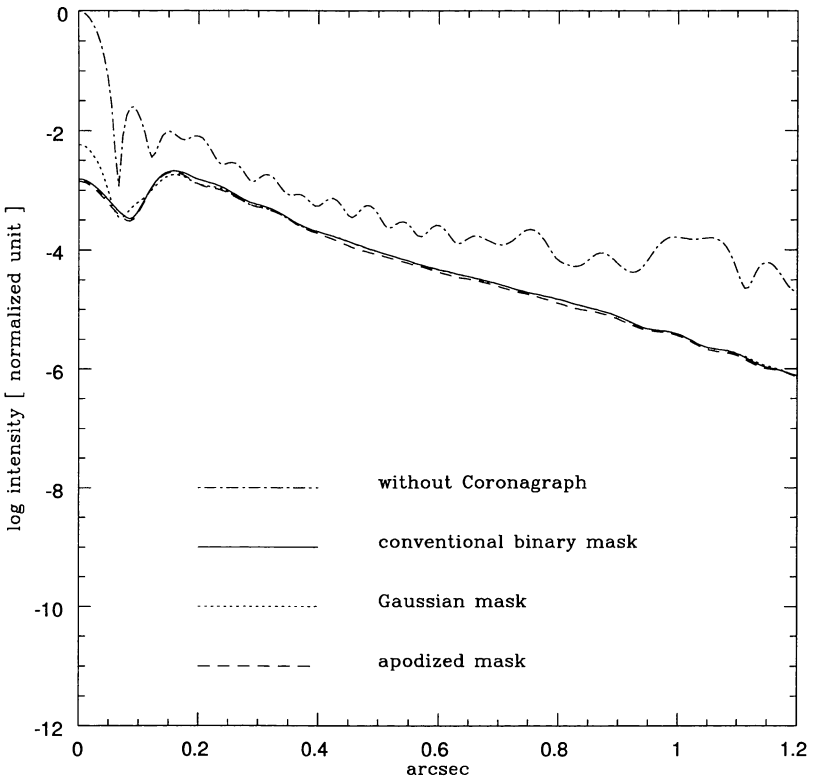

Fig. 4. Effect of the occulting mask simulated for a single point source. The dot-dashed line represents the PSF without a stellar coronagraph. The PSFs using a stellar coronagraph with the conventional binary mask, the Gaussian mask, and the apodized mask are shown by the solid line, the dot, and the dashed line, respectively. All masks have 0.″22 diameter. No significant differences are seen in the resultant PSFs, especially at the halo.

3.2. Apodized Lyot Stop

It has been emphasized that an apodized Lyot stop (Gaussian smoothed stop) diminishes the halo of the central source more effectively than does a classical unapodized Lyot stop (Jacquinot, Roizen-Dossier 1965; Nakajima 1994). We also confirm the effect of an apodized Lyot stop. We simulate a stellar coronagraphic observation for a single source taking into account any turbulence caused by the atmosphere and the telescope, in order to evaluate the effect of an apodized Lyot stop and to optimize the shape. The Lyot stop is assumed to be a Gaussian smoothed stop with a secondary mirror and its support patterns at the pupil. The amplitude transmittance of Gaussian smoothed pattern $T_{\rm l}(r)$ is given by

$$T_{\rm l}(r)=\left\{\begin{array}{ll}1 & \left(\text{for} \quad r \leq a\dfrac{D}{2}\right)\\ 0 & \left(\text{for} \quad r > a\dfrac{D}{2}\right)\end{array}\right\} * \exp\left[-\frac{r^2}{\left(b\dfrac{D}{2}\right)^2}\right], \quad (11)$$

where r is the distance from the center of the stop, D is the diameter of the entrance at the pupil plane, a is the effective diameter ratio of the Lyot stop, b is a constant, and $*$ means two-dimensional convolution. The pattern blocking the diffracted light caused by the secondary mirror and its support are also apodized. As mentioned by Malbet (1996), the shape of the most effective Lyot stop pattern depends on the size of the occulting mask. For an occulting mask of 0.″2 diameter, we find that a and b are 0.8 and 0.1, respectively, for the most effective Lyot stop. The resultant PSFs are shown in figure 5, where an apodized Lyot stop suppresses the halo more effectively than a classical unapodized Lyot stop.

4. Scientific Performance in Stellar Coronagraphic Observations

CIAO will be a powerful instrument for observing faint infrared objects in the very close vicinity of the central source. Such objects are common: brown dwarfs in binary systems, protoplanetary disks and extrasolar planets. We now present the results of our computer simulations for the observations of a brown dwarf in a binary system and a protoplanetary disk.

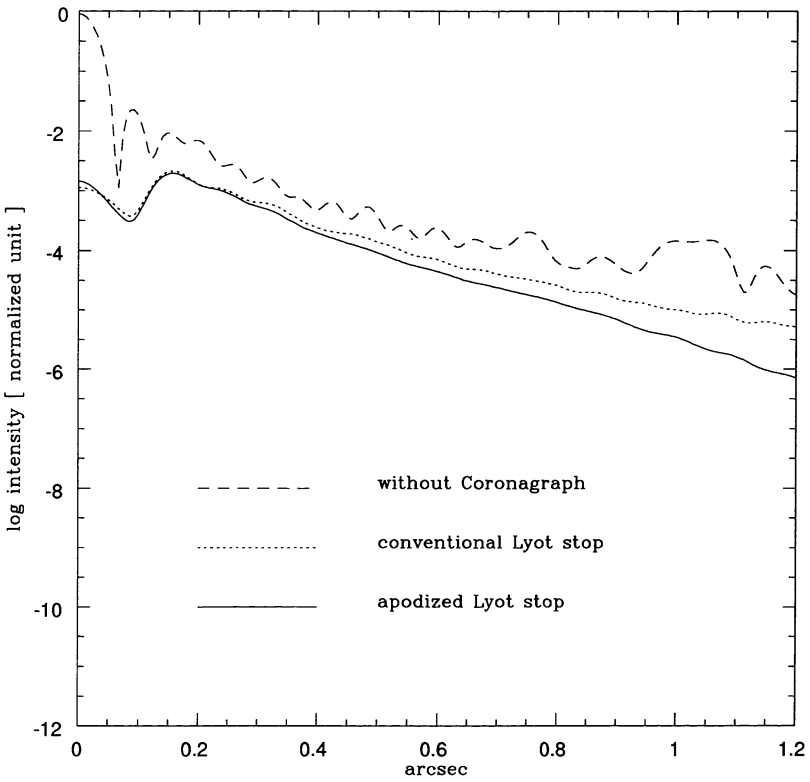

Fig. 5. Effect of various types of the Lyot stop simulated for a single point source. The dashed line represents the PSF without a stellar coronagraph. The dot and the solid lines represent the PSFs using a conventional unapodized Lyot stop and an apodized Lyot stop, respectively.

4.1. Young Brown Dwarf in a Binary System

The first definitive cold brown dwarf was discovered as a companion of a binary system (Gl 229B, Nakajima et al. 1995). Considering the fact that a number of main-sequence stars are in binary/multiple systems (Duquennoy, Mayor 1991), and that about one half of all young stellar objects in nearby dark clouds have companions (Simon et al. 1995), it is likely that many brown dwarfs form as companions in binary systems. Recent theories of binary formation (Shu et al. 1990; Bonnell et al. 1991; Pringle 1989) predict that a young binary system has a separation on the orders of 10 and 100 AU.

We now discuss the detectability of a brown dwarf in a binary system in the Pleiades cluster at a distance of 125 pc. Since the luminosity ratio of a primary to a brown dwarf is smaller for a younger binary system (e.g., D'Antona, Mazzitelli 1994), it is expected to be easier to detect a brown dwarf in a binary system located in a nearby star-forming region than in the Pleiades.

The simulated binary system consists of a primary star having the same K magnitude as Asterope ($m_K = 5.8$) in the Pleiades and a companion young brown dwarf with a mass of $0.05\,M_\odot$. The separation between the primary and the companion is assumed to be 75 AU. At the distance of the Pleiades, the apparent separation of this binary system is about $0''.6$. Since the age of the Pleiades is estimated to be about 7×10^7 yr (Stauffer et al. 1989), and there is little interstellar absorption (Stauffer et al. 1989; Simons, Becklin 1992), we estimate the apparent magnitude of this brown dwarf to be 14.9 mag at the K band, using the evolutionary track of D'Antona and Mazzitelli (1994) and the bolometric correction of Bessell (1991).

The K-band observation of such a binary system is simulated under the condition of seeing $D/r_0 = 5.0$, corresponding to 0.45 seeing at the V band. The series of observations consist of the observation of the binary system and that of a single star as a reference. We average iterations of 1000 times for each observation, which corresponds to about a few minute integrations, provided that the atmospheric fluctuation timescale is a few hundred milliseconds (Kataza, Maihara 1993). The deviation is about 1% of the halo intensity. Figure 6 shows radial-profiles of the coronagraphic observations for the binary system and a single star. A series of observations without a coronagraph were also simulated. The signal-to-noise ratio (SNR) of the brown dwarf for the stellar coronagraphic observation is about 400, which is improved by 5 compared with direct imaging without a coronagraph. In the calculation we assumed that the readout noise of

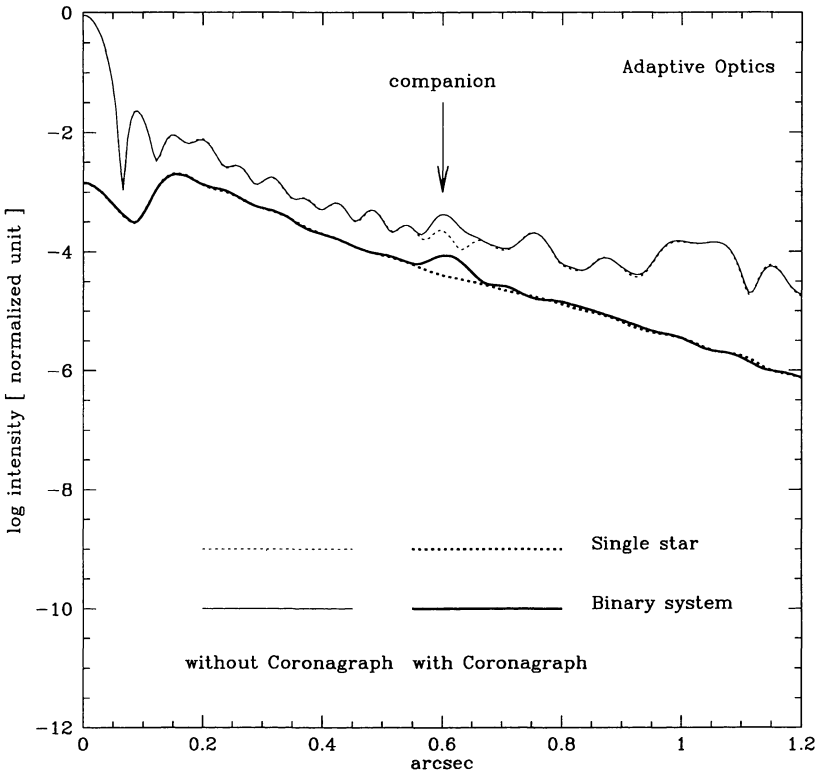

Fig. 6. Resultant intensity profiles of simulations for a young brown dwarf in the binary system. D/r_0=5.0 is assumed for the K band observation. The K-band magnitude of the primary star is 5.8, and the secondary is 14.9 mag. The separation between the primary and the secondary is assumed to be 75 AU. The apparent separation is about 0.″6, provided that the distance of the system is 125 pc. Each field of view is 2.″2 × 2.″2. The correction by the adaptive optics system corresponds up to the first 20th terms of Zernike expansion for all images. These results correspond a few minutes of integration observations. The thin lines represent the intensities without a stellar coronagraph, and the thick lines show with a stellar coronagraph. In both cases, the dot lines represent observations for single star, and the solid lines represent those for binary system.

the detector, Poisson noise of the sky background, and Poisson noise of the halo of the primary star are small and negligible compared with the fluctuation of the halo due to atmosphere, as is the case for the typical integration time (such as 30 s integration).

The K-band stellar coronagraphic observations of the binary system with only a tip-tilt system and without an adaptive optics system were also simulated under the same atmospheric condition. Figure 7a shows the radial profiles of the results for the tip-tilt observations, and figure 7b shows for the observations without any adaptive optics system. Both results correspond to a few minutes of integrations. With the tip-tilt system, the companion can be detected with one fourth the SNR of the stellar coronagraphic observation with the adaptive optics. Without any adaptive optics system, the SNR of the companion is smaller than unity, even if the coronagraph is used.

The FWHM of the primary star is 0.″055 using the adaptive optics system, whereas the FWHM is about 0.″27 for no compensation system. We can use a smaller occulting mask an the observation with adaptive optics system, compared with for an observation without any compensation.

4.2. Detectability of Companion Sources

Because the resultant intensity is the sum of the speckle patterns, the ratio of the background fluctuations to the background intensity due to atmospheric turbulence is almost constant at any portion of the halo. Therefore, the background fluctuation is proportional to the background intensity. The intensity of the companion object does not change at any separation unless obscured by the occulting mask; therefore, the SNR of the companion is inversely proportional to the halo intensity of the central primary object. The CIAO's performance was evaluated for detecting companions. This performance is shown in figure 8, in terms of the separation vs. brightness ratio. The phase space is hatched, where the companion can be detected with SNR = 3 in 2 minutes of integration. The companion whose separation is less than

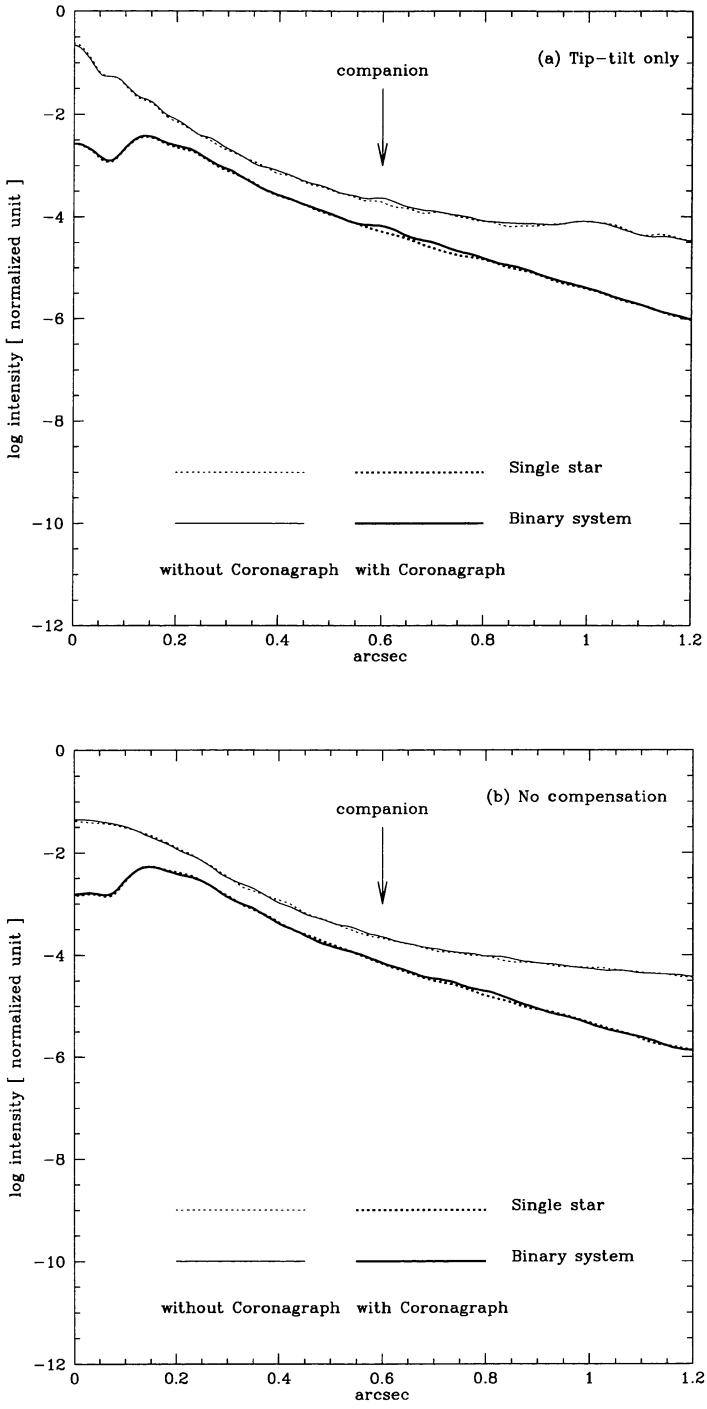

Fig. 7. Same as figure 6, except for only tip-tilt working instead of the adaptive optics (a), and except for neither adaptive optics nor tip-tilt working (b).

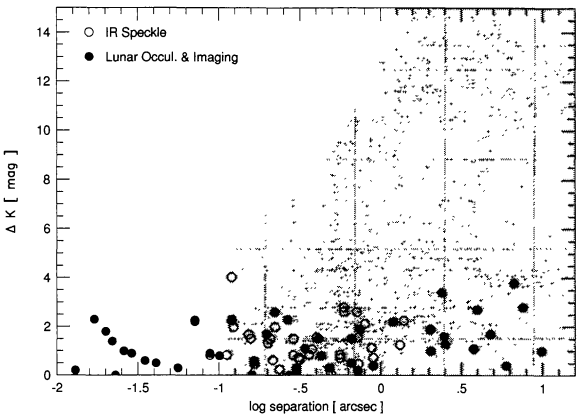

Fig. 8. K-band dynamic range (brightness ratio between the central source and companion vs. separation) of CIAO. The region of the stellar coronagraphic observation is shown by hatched area, where the point source is detected with SNR > 3 in 2 minutes integration. Also plotted are the binary systems which have been detected by near-infrared speckle observations (Ghez et al. 1993), by the lunar occultation observations, and by the direct imaging observations (Simon et al. 1995).

0.″11 to the primary star cannot be detected due to the 0.″22 diameter occulting mask. The young binary systems which have been detected to date by near-infrared speckle observations (Ghez et al. 1993), by observations using lunar occultation, or by direct imaging observations (Simon et al. 1995) are also shown. However, although for close systems consisting of two objects with similar luminosities, lunar occultations and speckle observations are powerful tools for resolving out these two objects, they are not suitable for detecting a faint object in the vicinity of the central bright star. In contrast, the stellar coronagraphic observation has a very large dynamic range. Clearly, stellar coronagraphic observations with the adaptive optics system have advantages for the observation of the binary systems having a very large brightness ratio between the companion and the primary.

4.3. Protoplanetary Disk

It has been suggested that 100 AU scale disks are ubiquitous around young stellar objects (YSOs ; Beckwith et al. 1990; Strom et al. 1989). Recent high-resolution observations have begun to directly reveal the protoplanetary disks by the Hubble Space Telescope (O'Dell, Wong 1996), and by the adaptive optics system (Close et al. 1997).

We simulated stellar coronagraphic observations of a protoplanetary disk around YSOs, in which the dust disk is seen in the scattered light from the central source. We employed the disk model of Lazareff, Pudritz, and Monin (1990). The density structure of the disk is based on the Shakura and Sunyaev (1973) model, which is given by

$$\rho(r,z) = \rho_{\rm d}\left(\frac{r_{\rm d}}{r}\right)^{-\alpha}\exp\left[\frac{-\pi z^2}{4h(r)^2}\right]^{\gamma}, \tag{12}$$

$$h(r) = \left(\frac{r}{r_{\rm d}}\right)^{\beta} z_{\rm d}, \tag{13}$$

where $\rho_{\rm d}$ and $z_{\rm d}$ are, respectively, the midplane density and the scale height at disk outer radius $r_{\rm d}$. We modeled a disk with an inner disk radius of 20 AU, $r_{\rm d} = 100$ AU, $z_{\rm d} = 25$ AU, $\rho_{\rm d} = 3.5 \times 10^{-16}$ g cm^{-3}, $\alpha = \frac{15}{8}$, $\beta = \frac{17}{8}$, $\gamma = 1$, and a system inclination of 55°. The inner and outer radii correspond to 0.″15 and 1″, respectively, assuming the distance of the Taurus molecular cloud is to be 140 pc. The radius of the central star was assumed to be $2\,R_{\odot}$. The dust grain model is the large grain model of Pendleten, Tielens, and Werner (1990) based on the size distribution of Mathis, Rumpl, and Nordsieck (1977). At near-infrared wavelengths, a protoplanetary disk emits mostly by scattered light of the central star (e.g., Bouvier et al. 1994). If single scattering paths contribute most of the emergent light and isotropic scattering, the emergent intensity of the disk is given by

$$I_\lambda(\mathcal{T}) = \int_{-\infty}^{+\infty} \frac{L_\lambda}{4\pi R^2} e^{-\tau_1}\rho(\boldsymbol{R})\frac{\kappa_{\rm s}}{4\pi}e^{-\tau_2}du, \tag{14}$$

where $\boldsymbol{R}$ is the location of a scattering grain, R is the distance from the star, u is the optical axis along a ray $\mathcal{T}$ reckoned positive toward the observer, τ_1 and τ_2 are the optical depths from the central star to $\boldsymbol{R}$, and from $\boldsymbol{R}$ to the observer, respectively. τ is given by

$$\tau = \int \rho(\kappa_{\rm a} + \kappa_{\rm s})du, \tag{15}$$

where $\kappa_{\rm a}$ and $\kappa_{\rm s}$ are, respectively, the absorption and scattering opacities.

In the calculation, the intensity of the disk was 10-times brighter than that calculated from equation (14). An iteration of 1000 times was carried out. If a long term variation of the PSF mainly due to seeing can be eliminated by frequent observations of a single star, this simulated observation corresponds to ten hours of integration at the K band under the condition $D/r_0 = 3.0$ (about 0.″3 seeing condition at V). Figure 9 (Plate 2) shows the resulting images with and without a stellar coronagraph. Both images are divided by the image of a single star. The outer region of the disk is revealed only in the case of the stellar coronagraphic observation, while the inner region is not detected in both cases because of high background due to the halo of the central star. Stellar coronagraphic observations are useful for not only point-like sources, but also for extended objects, such as protoplanetary disks.

5. Conclusion

We have carried out the computer simulations for CIAO (Coronagraphic Imager with Adaptive Optics) on the Subaru 8 m telescope in order to optimize the shapes and sizes of occulting masks and Lyot stops and to evaluate the performance of the stellar coronagraphic camera for astronomical objects. The calculations took into account of atmospheric turbulence as well as surface errors of the telescope primary mirror. The wavefront was expanded in terms of Zernike polynomials. We find that the higher order terms of Zernike expansion affect the resultant PSFs significantly, which was omitted in previous studies, and that they should be included in simulations for stellar coronagraphic observations. CIAO will be a powerful instrument for studying many astronomical objects, particularly for a brown-dwarf search in binary systems. It will also be useful for studying faint extended objects nearby the central source, including the protoplanetary disks.

The authors thank M. Otsubo and K. Murakawa for many useful discussions concerning the computer simulations. We also thank N. Kaifu and T. Nakajima for useful comments, and C. Packham for reading the manuscript. Y.I. acknowledges support from JSPS Research Fellowships.

References

Beckwith S.V.W., Sargent A.I., Chini R.S., Gusten R. 1990, AJ 99, 924
Bessell M.S. 1991, AJ 101, 662
Bonnell I., Martel H., Bastien P., Arcoragi J., Bentz W. 1991, ApJ 377, 553
Bouvier J., Malbet F., Monin J.L. 1994, Ap&SS 212, 159
Breckinridge J.B., Kuper T.G., Shark R.V. 1982, Proc. SPIE 331, 395
Close L.M., Roddier F., Northcott M.J., Roddier C., Graves E. 1997, ApJ 478, 766
D'Antona F., Mazzitelli I. 1994, ApJS 90, 467
Duquennoy A., Mayor M. 1991, A&A 248, 455
Fried D.L. 1965, J. Opt. Soc. Am. 55, 1427
Ftaclas C., Nonnenmacher A.L., Terrile R.J., Pravdo S.H., Gatewood G.D., Levy E.H. 1994, Ap&SS 212, 441
Ghez A.M., Neugebauer G., Matthews K. 1993, AJ 106, 2005
Golimowski D.A., Clampin M., Durrance S.T., Barkhouser R.H. 1992, Appl. Opt. 31, 4405
Jacquinot P., Roizen-Dossier B. 1964, in Progress in Optics, ed E. Wolf (North Holland Publ., Amsterdam) vol3, p31
Kataza H., Maihara T. 1993, PASP 105, 432
Lazareff B., Pudritz R.E., Monin J.L. 1990, ApJ 358, 170
Lyot B. 1939, MNRAS 99, 580
Malbet F. 1996, A&AS 115, 161
Malbet F., Yu J.W., Shao M. 1995, PASP 107, 386
Mathis J.S., Rumpl W., Nordsieck K.H. 1977, ApJ 137, 202
Nakajima T. 1994, ApJ 425, 348
Nakajima T., Haniff C.A. 1993, PASP 105, 509
Nakajima T., Oppenheimer B.R., Kulkarni S.R., Golimowski D.A., Matthews K., Durrance S.T. 1995, Nature 378, 463
Noll R.J. 1976, J. Opt. Soc. Am. 66, 207
O'Dell C.R., Wong S.K. 1996, AJ 111, 846
Pendleton Y.J., Tielens A.G.G.M., Werner M.W. 1990, ApJ 349, 107
Pringle J.E. 1989, MNRAS 239, 361
Roddier N. 1990, Opt. Eng. 29, 1174
Shakura N.I., Sunyaev R.A. 1973, A&A 24, 337
Shu F.H., Tremaine S., Adams F.C., Ruden S.P. 1990, ApJ 358, 495
Simon M., Ghez A.M., Leinert Ch., Cassar L., Chen W.P., Howel R.R., Jameson R.F., Matthews K. et al. 1995, ApJ 443, 625
Simons D.A., Becklin E.E. 1992, ApJ 390, 431
Smith A., Terrile R.J. 1984, Science 226, 1421
Stauffer J., Hamilton D., Probst R., Rieke G., Mateo M. 1989, ApJ 344, L21
Strom K.M., Strom S.E., Edwards S., Cabrit S., Skrutskie M.F. 1989, AJ 97, 1451
Takami H., Iye M., Takato N., Otsubo M., Kanzawa T., Nakashima K. 1997, Proc. SPIE 2871, 953
Tamura M., Takami H., Kaifu N., Hayashi S., Takato N., Nishimura T., Murakawa K., Itoh Y. 1995, in Scientific and Engineering Frontiers for 8–10 m Telescope, ed M. Iye, T. Nishimura (Universal Academy Press, Tokyo) p339

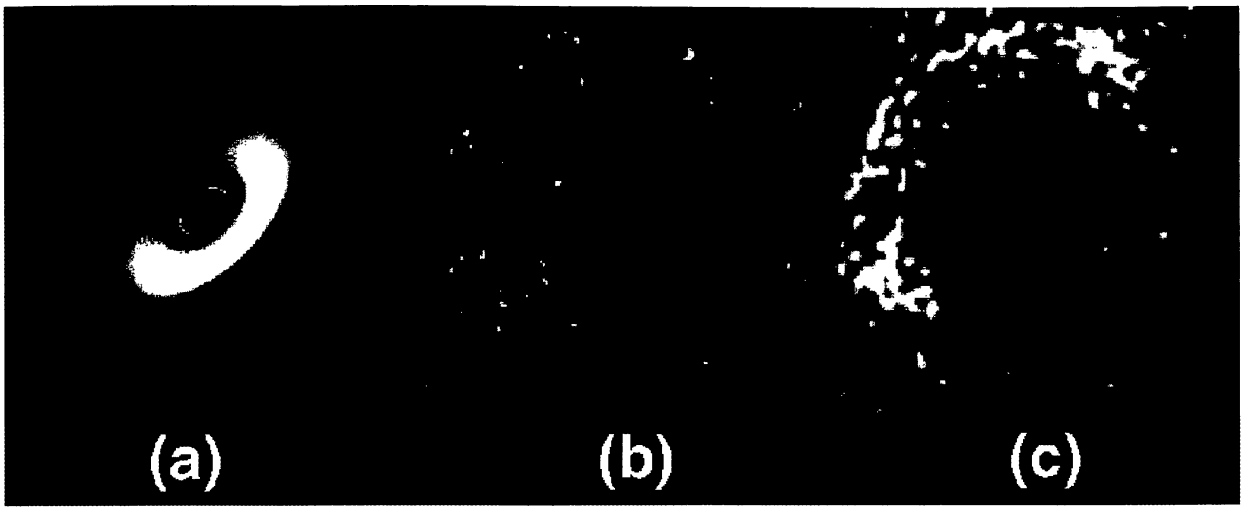

Fig. 9. Resultant images of simulations for 10 hours of integrated observation of the protoplanetary disk around the young stellar object under a seeing condition of $D/r_0 = 3.0$. (a) Intensity of the simulated disk. (b) Focal-plane image without stellar coronagraph, which is divided by the image of single point star. The disk is hardly seen. (c) Stellar coronagraph image, which is also divided by the image of single point star. An outer part of the disk is clearly seen, using only the stellar coronagraph.